# Polarization control with dielectric helix metasurfaces and arrays

## ILKER KARAKASOGLU, MENG XIAO, AND SHANHUI FAN

Department of Electrical Engineering, Stanford University, Stanford, California 94305, USA \*shanhui@stanford.edu

**Abstract:** Using band structure analysis and reflectance spectrum simulations, we show that dielectric helices exhibit strong circular dichroism and have polarization stop gaps for light propagating perpendicular to the helices, despite the lack of helical symmetry along this direction. We apply perturbation theory to quantitatively explain these effects. We also demonstrate that even for a single layer of dielectric helices similar phenomena exist. As a result, the helix array can operate as a dielectric chiral mirror. This dielectric chiral mirror can completely reflect normally incident light with one circular polarization (right- or left-handed as determined by the handedness of the helices) without changing the polarization's handedness while allowing light with the opposite circular polarization to be entirely transmitted.

© 2018 Optical Society of America under the terms of the OSA Open Access Publishing Agreement

OCIS codes: (160.1585) Chiral media; (160.3918) Metamaterials; (230.4040) Mirrors; (240.5440) Polarization-selective devices.

#### References and links

- 1. J. B. Pendry, "A chiral route to negative refraction," Science 306, 1353–1355 (2004).
- S. L. Prosvirnin and N. I. Zheludev, "Polarization effects in the diffraction of light by a planar chiral structure," Phys. Rev. E 71, 037603 (2005).
- 3. M. Thiel, M. Decker, M. Deubel, M. Wegener, S. Linden, and G. von Freymann, "Polarization stop bands in chiral polymeric three-dimensional photonic crystals," Adv. Mater. 19, 207–210 (2007).
- H. Liu, D. A. Genov, D. M. Wu, Y. M. Liu, Z. W. Liu, C. Sun, S. N. Zhu, and X. Zhang, "Magnetic plasmon hybridization and optical activity at optical frequencies in metallic nanostructures," Phys. Rev. B 76, 073101 (2007).
- Y. Zhao, M. Belkin, and A. Alù, "Twisted optical metamaterials for planarized ultrathin broadband circular polarizers," Nat. Commun. 3, 870 (2012).
- Z. Li, M. Mutlu, and E. Ozbay, "Chiral metamaterials: from optical activity and negative refractive index to asymmetric transmission," J. Opt. 15, 023001 (2013).
- Z. Wang, F. Cheng, T. Winsor, and Y. Liu, "Optical chiral metamaterials: a review of the fundamentals, fabrication methods and applications," Nanotechnology 27, 412001 (2016).
- 8. C. Wu, H. Li, Z. Wei, X. Yu, and C. T. Chan, "Theory and experimental realization of negative refraction in a metallic helix array," Phys. Rev. Lett. **105**, 247401 (2010).
- 9. C. Wu, H. Li, X. Yu, F. Li, H. Chen, and C. T. Chan, "Metallic helix array as a broadband wave plate," Phys. Rev. Lett. 107, 177401 (2011).
- 10. J. Hu, X. Zhao, Y. Lin, A. Zhu, X. Zhu, P. Guo, B. Cao, and C. Wang, "All-dielectric metasurface circular dichroism waveplate," Sci. Rep. 7, 41893 (2017).
- 11. A. Chutinan and S. Noda, "Spiral three-dimensional photonic-band-gap structure," Phys. Rev. B 57, 2006 (1998).
- O. Toader and S. John, "Proposed square spiral microfabrication architecture for large three-dimensional photonic band gap crystals," Science 292, 1133–1135 (2001).
- S. Erten, A. Lakhtakia, and G. D. Barber, "Experimental investigation of circular Bragg phenomenon for oblique incidence," J. Opt. Soc. Am. A 32, 764–770 (2015).
- 14. J. C. W. Lee and C. T. Chan, "Polarization gaps in spiral photonic crystals," Opt. Express 13, 8083–8088 (2005).
- 15. T.-H. Kao, L.-Y. C. Chien, and Y.-C. Hung, "Dual circular polarization gaps in helix photonic metamaterials," Opt. Express 23, 24416–24425 (2015).
- 16. H.-T. Tung, Y.-K. Chen, P.-L. Jheng, and Y.-C. Hung, "Origin and manipulation of band gaps in three-dimensional dielectric helix structures," Opt. Express 25, 17627–17638 (2017).
- Y. Liu, Z. Yan, Q. Lin, X. Guo, M. Han, K. Nan, K.-C. Hwang, Y. Huang, Y. Zhang, and J. A. Rogers, "Guided formation of 3D helical mesostructures by mechanical buckling: Analytical modeling and experimental validation," Adv. Funct. Mater. 26, 2909–2918 (2016).
- 18. S. Lee, B. Kang, H. Keum, N. Ahmed, J. A. Rogers, P. M. Ferreira, S. Kim, and B. Min, "Heterogeneously assembled metamaterials and metadevices via 3D modular transfer printing," Sci. Rep. 6, 27621 (2016).

- 19. S. G. Johnson and J. D. Joannopoulos, "Block-iterative frequency-domain methods for Maxwell's equations in a planewave basis," Opt. Express 8, 173–190 (2001).
- S. Sandhu and S. Fan, "FDTD Plus," http://stanford.wikia.com/wiki/FDTD\_Plus. Accessed: 2018-01-10.
- 21. M. Skorobogatiy and J. Yang, Fundamentals of Photonic Crystal Guiding (Cambridge University, 2009).
- S. G. Johnson, M. Ibanescu, M. A. Skorobogatiy, O. Weisberg, J. D. Joannopoulos, and Y. Fink, "Perturbation theory for Maxwell's equations with shifting material boundaries," Phys. Rev. E 65, 066611 (2002).
- 23. E. Plum and N. I. Zheludev, "Chiral mirrors," Appl. Phys. Lett. 106, 221901 (2015).
- 24. L. Kang, S. P. Rodrigues, M. Taghinejad, S. Lan, K.-T. Lee, Y. Liu, D. H. Werner, A. Urbas, and W. Cai, "Preserving spin states upon reflection: linear and nonlinear responses of a chiral meta-mirror," Nano Lett. 17, 7102–7109 (2017).
- Y. Guo, M. Xiao, and S. Fan, "Topologically protected complete polarization conversion," Phys. Rev. Lett. 119, 167401 (2017).

#### 1. Introduction

Three-dimensional chiral metamaterials have been extensively explored for a wide variety of unusual optical effects such as circular dichroism, polarization stop gaps, optical activity and negative refractive index [1–7]. The majority of existing three-dimensional chiral structures utilizes metals [7–9]. On the other hand, there is also interest of exploring dielectric chiral metamaterials since dielectric has lower loss in the optical frequencies [7, 10].

A natural way to create a three-dimensional chiral dielectric metamaterial is to use a two-dimensional array of dielectric helices. An example of such a system is shown in Fig. 1, which consists of a square lattice of helices whose band structure has been previously considered [11]. Such a metamaterial can be experimentally fabricated with techniques such as direct laser writing [3], angle deposition [12] and thermal evaporation [13]. For the applications of such metamaterials it is thus important to develop a theoretical understanding. Existing theoretical works on three-dimensional chiral dielectric metamaterials have mostly focused on light propagating along the axis of the helices [14–16]. This focus is natural since along the axis direction the effect of circular dichroism can be easily understood from the helical symmetry. On the other hand, the recent experiments demonstrated by Liu et al. in [17] and Lee et al. in [18] created helices with their axis parallel to a substrate. For such experimental systems, it would be of interest to understand the behavior of light propagating along the direction perpendicular to the helices as well.

In this paper, using band structure analysis and finite-difference time-domain simulations, we show that for the structure shown in Fig. 1, there are pronounced effects of circular dichroism and polarization stop gaps along the direction perpendicular to the helices, in spite of the fact that there is no helical symmetry of the structure along this direction. We develop a perturbation theory formalism that completely accounts for these effects. Moreover, we show that these effects in fact persist even in a single layer of one-dimensional array of helices, which is a metasurface. These effects enable the creation of a dielectric chiral mirror for normally incident light, for which the reflectivity can reach 100%, and the handedness of light is preserved during the reflection. This is in contrast with regular mirrors for which the handedness flips in the reflection process.

The rest of the paper is organized as follows: In Section 2, we introduce an exemplary structure. In Section 3, we characterize the band structure and the eigenmodes of the structure discussed in Section 2. We also numerically calculate the reflectance spectra of light that is normally incident on finite number of layers of helices. We compare and contrast the results for the direction perpendicular to the helices and the results for the direction parallel to the helices. In Section 4, we provide field plots to visualize the chirality of the eigenmodes. In Section 5, we use perturbation theory to give a quantitative explanation of the chirality of the eigenmodes propagating perpendicular to the helices. In Section 6, we demonstrate the use of a single layer of helices as a a chiral mirror. We conclude in Section 7.

## 2. Structure description

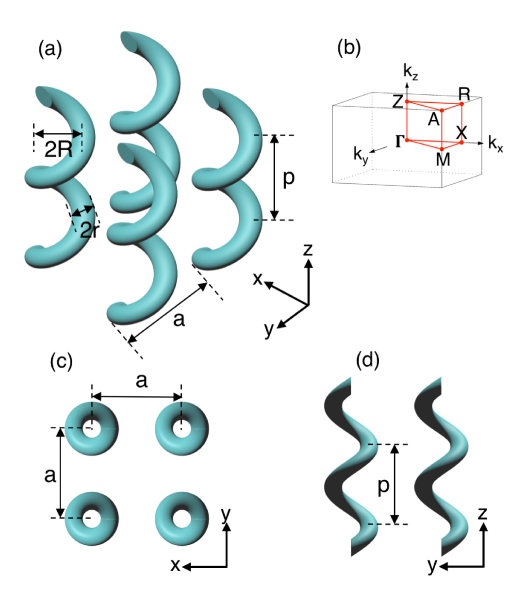


Fig. 1. (a) is a schematic diagram of a helix array which is parameterized by the lattice constant a, pitch length p, wire radius r and helix radius R. We specifically worked with right-handed helices that have p=1.29a, r=0.13a and R=0.29a. Helices are made of silicon ( $\varepsilon_{helix}=11.7$ ) and the host medium is air ( $\varepsilon_{host}=1$ ). We consider N number of helices for reflectance calculations for the direction of propagation perpendicular to the helices (the  $\Gamma X$  direction). A metasurface has N=1 and a helix array has  $N=\infty$ . (b) shows the points of interest in the first Brillouin zone. (c) and (d) are, respectively, the views along the helix axis and along the x axis.

Figure 1 illustrates a schematic of the helix structure under study. It consists of right-handed helices whose axes lie parallel to the z axis and forms a square lattice in the xy plane. There are four parameters that define the geometry of the structure: lattice constant a, pitch length p, wire radius r and helix radius R. We make our calculations with p = 1.29a, r = 0.13a and R = 0.29a, which were chosen to maximize the circular polarization dependent characteristics. Helices are made of silicon and embedded in air, whose relative permittivities are  $\varepsilon_{helix} = 11.7$ and  $\varepsilon_{host} = 1$ , respectively. We assume the incident light is in the frequency range below the silicon band gap, for example the frequency range of 10-100 THz, where silicon is not absorbing and the permittivity of silicon varies less than 1% around 11.7 so it can be taken as a constant. For band structure and eigenmode analyses, we use the software MPB [19]. For reflectance and transmittance calculations, we use an open-source finite-difference finite-domain (FDTD) solver [20]. Our simulation procedures for calculating the components of linear and circular polarizations are briefly described as following: there are two independent polarizations for the incident light along the x direction. Hence we calculate the complex-valued reflectance and transmittance with the electric field of the input light linearly polarized along the y and z directions independently. The reflection and transmission coefficients of any other polarization is a linear combination of the y and z linearly polarized lights. Accordingly, we transform the reflectance and transmittance calculated for these two linear polarizations to determine the reflectance and transmittance for circular polarizations, as will be later presented in Fig. 2.

#### 3. Band structure and reflectance spectrum

We start our analysis by characterizing the band structure and the eigenmodes for the structure illustrated in Fig. 1, assuming it is periodic in all three directions. The goal here is to understand the chirality of the eigenmodes and how strongly a given eigenmode favors one circular polarization over the other. Figure 1(b) displays the first Brillouin zone with some high symmetry points labeled. We contrast the  $\Gamma X$  direction, where light is propagating perpendicular to the helices, with the  $\Gamma Z$  direction, where light is propagating along the helix axis.

There are two main variables that characterize the chirality of an eigenmode: circular dichroism index (CD index) and coupling index ( $\kappa$ ). CD index is a measure of the degree of how much an eigenmode is right- or left-handed circularly polarized [14, 15]. The polarization of any electromagnetic wave can be written as a linear combination of left-handed circular polarization (LCP) and right-handed circular polarization (RCP). The CD index ranges from -1 for LCP to +1 for RCP and is defined as

$$CD = \operatorname{sgn}(\vec{k} \cdot \nabla_k \omega) \frac{\eta_{RCP} - \eta_{LCP}}{\eta_{RCP} + \eta_{LCP}}$$
(1)

where  $\vec{k}$  is the wave vector of the eigenmode. In Eq. (1), the first term on the right hand side gives the sign of the propagation direction as determined by the direction of the group velocity.  $\eta_{RCP}$  and  $\eta_{LCP}$  are the normalized circular polarization coupling coefficients. For the eigenmodes with the wave vectors along the  $\Gamma X$  direction, they are calculated by evaluating the overlap integrals between the magnetic field  $\vec{H}(x_0, y, z)$  of the Bloch modes at  $x = x_0$  plane and a circularly polarized wave described by  $(\hat{y} - i\hat{z})/\sqrt{2}$  or  $(\hat{y} + i\hat{z})/\sqrt{2}$  for RCP and LCP, respectively.  $\eta_{RCP(LCP)}$  varies slightly depending on the position of the cross-section plane  $x_0$ , so we average over all  $x_0$  in a unit cell as

$$\eta_{RCP(LCP)} \equiv \frac{\left| \int \int \int \left[ \frac{1}{\sqrt{2}} (\hat{y} \mp i\hat{z}) \right] \cdot \vec{H}(x, y, z) dx dy dz \right|^2}{V \int \int \int |\vec{H}(x, y, z)|^2 dx dy dz}, \tag{2}$$

where V is the volume of the unit cell and the integration is done over the entire unit cell.  $\eta_{RCP(LCP)}$  for the eigenmodes propagating along the  $\Gamma Z$  direction are defined similarly. We note that either electric or magnetic fields can be used in the circular polarization descriptions and the calculations of  $\eta_{RCP(LCP)}$ . In Eq. (2), however, we use magnetic fields instead of electric fields because electric fields have discontinuities at dielectric boundaries while magnetic fields do not.

The coupling index  $(\kappa)$  is the second variable that is used to characterize chirality.  $\kappa$  measures the ability of a plane wave to be coupled into a given eigenmode. It is calculated as

$$\kappa = \eta_{RCP} + \eta_{LCP}.\tag{3}$$

Because RCP and LCP are orthogonal to each other and  $\eta_{RCP(LCP)}$  are normalized,  $\kappa$  ranges from 0 for no coupling to 1 for perfect coupling. Because  $\kappa$  measures the strength of coupling for any polarization, it is only used together with the CD index when analyzing chirality.

In the spirit of putting forward a cohesive analysis of dielectric helices, we first replicate the previous results of Kao et al. in [15] on the propagation parallel to the helix axis. Chirality emerges naturally in this case as the dielectric helix can guide the wave to form a helical wave of propagation. This feature is also reflected on the band structure as shown in Fig. 2(b). Here the circular markers on the bands describe eigenmodes and their polarization characteristics. Right-handed elliptically polarized eigenmodes, which have a positive CD index, are denoted in red tones and left-handed elliptically polarized eigenmodes, which have a negative CD index, are denoted in blue tones. The size of a marker indicates the coupling index  $\kappa$  of that eigenmode. The lowest four bands are almost perfectly left- or right-handed circularly polarized as can be

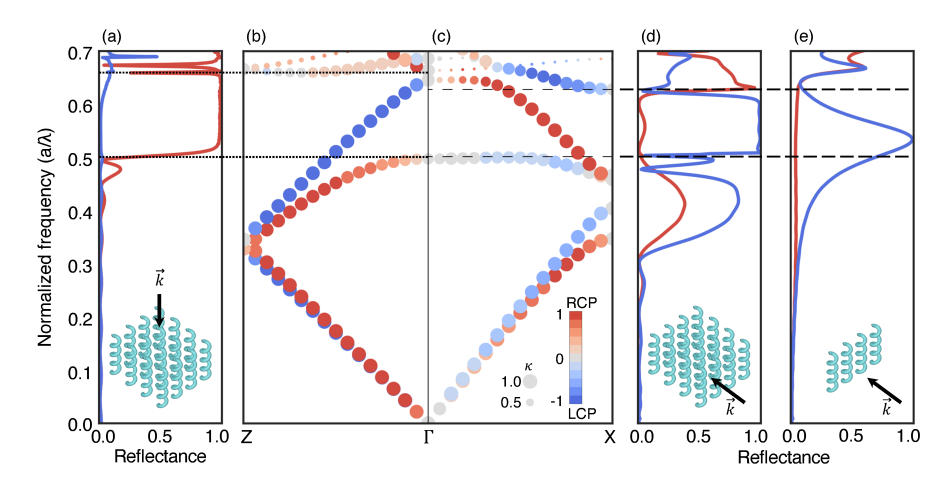


Fig. 2. (a) The intensity reflectance spectrum for incident light parallel to the helix axis (z axis). There are 4 turns of helices in this direction and the structure is periodic in x and y directions. (b) The band structure along the  $\Gamma Z$  direction and (c) along the  $\Gamma X$  direction of the helix array illustrated in Fig. 1. The markers on bands characterize the eigenmodes whose CD indices are denoted by the color and coupling indices are represented by the size of the markers. (d) and (e) are the reflectance spectra for propagation along the  $\Gamma X$  direction for the helix stacks of N=4 layers and N=1 layer, respectively. The helices are periodic in the z direction in (d) and (e). In (a), (d), and (e), red and blue lines represent the reflectance spectra when the incident light are of RCP or LCP, respectively.

seen from the color code. Meanwhile, there exists a frequency region (bounded by the two dotted lines) wherein only the eigenmodes with LCP are supported which indicates the existence of a polarization gap [8]. We also calculate the intensity reflectance spectrum of a finite system (4 turns of helices in the z direction) as shown in Fig. 2(a), where the red and blue curves represent the reflectance when the incident waves have RCP and LCP, respectively. As expected, light with RCP is almost totally reflected inside the polarization gap.

However, the direction of incident light being parallel to the helix axis is not the only case where the helix array exhibits a strong chiral response. In Fig. 2(c), we show the band structure along the  $\Gamma X$  direction, which describes the property of the system when the incident direction is perpendicular to the helices. Similar to the eigenmodes shown in Fig. 2(b), the eigenmodes in Fig. 2(c) are also strongly circularly polarized. Moreover, there also exists a frequency range between the two dashed lines wherein the system only supports the eigenmodes with RCP. This region's lower frequency boundary is marked by the maximum of the third band which has eigenmodes that are either linearly polarized (gray markers) or left-handed elliptically polarized. The upper frequency edge is bounded by the fifth band which favors left-handed elliptically polarized eigenmodes. A direct consequence of having such a frequency region that favors one particular circular polarization can be seen in the reflectance spectra. For the reflectance spectrum calculations along the  $\Gamma X$  direction, we assume that the structure is periodic in the y and z directions and regard the helices on the same yz plane as forming a single layer. In this direction of propagation, the x axis, we take N layers of helices. For a stack of N = 4 layers, the incident light with LCP is nearly perfectly reflected while the incident light with RCP is transmitted with almost no reflection in the region bounded by the dashed lines as shown in Fig. 2(d). We observe this clear region of high reflectance of LCP for stacks of 4 or more layers. Interestingly, this high reflectance is preserved even for a single layer (N = 1), which is a metasurface, as shown in Fig. 2(e). There is again almost 100% reflectance of the incident light with LCP but in a narrower frequency region.

## 4. Field plots

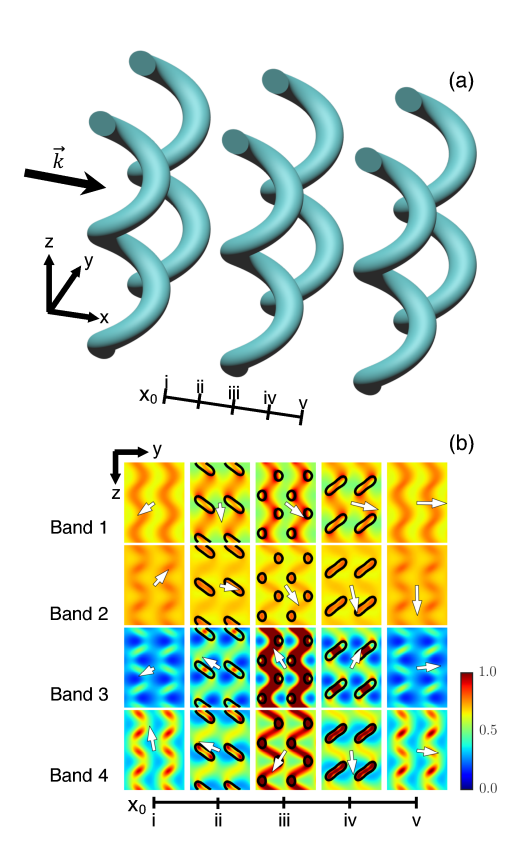


Fig. 3. (a) Cross sections are taken along the direction of propagation given by  $x_0$  (i, ii, iii, iv, v). (b) The magnetic field intensities of the first four bands' eigenmodes for the wave vector  $\vec{k} = (0.3, 0, 0)2\pi/a$ . The length and the direction of the white arrow on each cross section show the average magnetic field's intensity and direction, respectively. Tracing the arrows one can see that the fields rotate either in the clockwise (for left-handed elliptically polarized) or counter-clockwise (for right-handed elliptically polarized) direction. Bands 1 and 4 are predominately right-handed elliptically polarized while bands 2 and 3 are predominately left-handed elliptically polarized by the eigenmode analysis shown in Fig. 2(c).

The magnetic field distributions for the eigenmodes in the first four bands are presented in Fig. 3(b) for the cross-sections taken along the x axis as shown in Fig. 3(a). For each band, we plot the field distributions corresponding to the wave vector  $\vec{k} = (0.3, 0, 0)2\pi/a$ . The intensity and the direction of the real magnetic field averaged over a given cross section are denoted by the length and the direction of an arrow, respectively. The average real field intensity does not change significantly across different cross sections. On the other hand, as the wave propagates, the average real field direction rotates clockwise or counter-clockwise for left- and right-handed elliptically polarized eigenmodes, respectively. We plot the magnetic fields rather than the electric fields because of the discontinuous nature of electric field distributions caused by the large difference between  $\varepsilon_{helix} = 11.7$  and  $\varepsilon_{host} = 1$ . The plots in Fig. 3(b) provide a direct visualization of the chiral nature of the eigenmodes in the system.

### 5. Perturbation theory

To quantitatively understand how the elliptical polarization state emerges for propagation along the  $\Gamma X$  direction, in this section we provide a discussion by connecting the behavior of the array of helices to the behavior of the array of straight rods using perturbation theory. We consider the array of rods that has the same structural parameters  $(a, r, \varepsilon_{host}, \varepsilon_{rod} = \varepsilon_{helix})$  as those of the array of helices in our study. For the helical structure, the center of the helix wire is described by the following equation of a helical trajectory:

$$x(t) = R \cdot cos(t),$$
  

$$y(t) = R \cdot sin(t),$$
  

$$z(t) = \frac{p}{2\pi}t,$$
(4)

where R and p are, respectively, the radius and the pitch of the helical trajectory, and t is the coordinate along the trajectory. When R = 0 (for any p), the helical trajectory becomes a straight line. Accordingly, we employ R (for fixed p = 1.29a) as a tuning parameter to control the chirality in a structure.

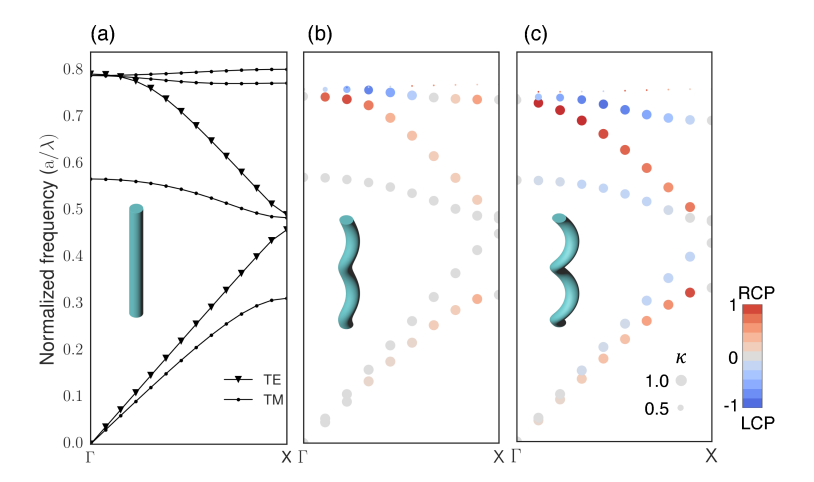


Fig. 4. The band structures of the rod array (a) and the helix arrays with (b) R = 0.07a and (c) R = 0.14a. As R increases, the chirality increases. The eigenmodes, as a result, become more elliptically polarized. In (b) and (c), the CD indices and the coupling indices of the eigenmodes are denoted by the markers' color and size, respectively.

In Fig. 4, we show the band structures of three arrays that only differ by R. The band structure in Fig. 4(a) is of such an array of straight rods (R=0). Its bands can be classified as either transverse-electric (TE) or transverse-magnetic (TM), where TE bands have magnetic fields solely along the z axis and TM bands have electric fields solely along the z axis. When R is increased from 0, the structure transforms from an array of rods to an array of helices. Figure 4(b) shows the band structure corresponding to R=0.07a. Compared to the band structure of the rod array, we see that the eigenmodes in general acquire chiral characteristics. This is in contrast with the bands in Fig. 4(a) where the bands are either TE or TM and hence non-chiral. On the other hand, the overall shape of the band structure in Fig. 4(b) strongly resembles that in Fig. 4(a). This observation, that chirality develops for  $R \neq 0$ , but the shape of the bands resemble those of the array of rods, persists as we further increase R, as shown in Fig. 4(c) where R=0.14a.

The observation in Fig. 4, about the similarity between the band structures of the array of rods and the array of helices, strongly suggests that one can quantitatively understand the band

structure of the array of helices using perturbation theory starting from the band structure of the array of rods. We apply perturbation theory assuming the following: (i) The rod array is the unperturbed system, (ii) the helix array is the perturbed system, (iii) the perturbation is defined by a small change  $\Delta \varepsilon$  due to shifting dielectrics caused by chirality, and (iv) R characterizes the strength of the perturbation.

The eigenmodes of a perturbed system can be expanded in terms of the eigenmodes of an unperturbed system [21]:

$$|E_i\rangle = |E_i^0\rangle + \sum_{j\neq i} \frac{\langle E_j^0 | \Delta \varepsilon | E_i^0 \rangle}{\omega_{0,i}^2 - \omega_{0,j}^2} |E_j^0\rangle, \tag{5}$$

where we use the Dirac notation for eigenmodes and inner products.  $|E_i^0\rangle$  is the *i*-th normalized eigenmode of the unperturbed system with the normalized eigenfrequency  $\omega_{0,i}$  and  $|E_i\rangle$  is the perturbed system's *i*-th normalized eigenmode. The normalization is defined as  $\langle E_i^0|\varepsilon|E_j^0\rangle = \delta_{i,j}$  where  $\delta_{i,j}$  is the Kronecker delta and  $\varepsilon$  is the position-dependent relative permittivity of the unperturbed system.  $\Delta \varepsilon$  is the perturbing Hamiltonian.

In Eq. (5), the calculation of the inner product  $\langle E_j^0|\Delta\varepsilon|E_i^0\rangle$  requires special attention. When the perturbation involves the shift of dielectric boundaries, the discontinuity of the perpendicular electric field components needs to be taken into account carefully [22]. We adopt the smoothing technique given by Johnson et al. in [22] to express  $\langle E_i^0|\Delta\varepsilon|E_i^0\rangle$  as a surface integral:

$$\langle E_j^0 | \Delta \varepsilon | E_i^0 \rangle = \int dA \frac{dh}{dR} \left[ \varepsilon_{||} (\mathbf{E}_{j-||}^{0*} \cdot \mathbf{E}_{i-||}^0) - \varepsilon_{\perp}^{-1} (\mathbf{D}_{j-\perp}^{0*} \cdot \mathbf{D}_{i-\perp}^0) \right], \tag{6}$$

where  $\varepsilon_{||} = \varepsilon_{helix} - \varepsilon_{host}$  and  $\varepsilon_{\perp}^{-1} = \varepsilon_{helix}^{-1} - \varepsilon_{host}^{-1}$ . h is the shifted distance of the dielectric boundary (between  $\varepsilon_{helix}$  and  $\varepsilon_{host}$ ) towards  $\varepsilon_{host}$ .  $\mathbf{E}_{\perp}$  ( $\mathbf{D}_{\perp}$ ) and  $\mathbf{E}_{||}$  ( $\mathbf{D}_{||}$ ) are the electric (displacement) field components that are normal and parallel to the dielectric boundary, respectively. \* stands for the conjugation operation. We remark that the use of  $\varepsilon_{||}$  and  $\varepsilon_{\perp}$  in Eq. (6), as detailed by Johnson et al. in [22], does not arise due to the homogenization of the dielectric helix array, but rather is based on a smoothing technique applied at the dielectric-air interface at the surface of the helix. This smoothing technique avoids the discontinuous transition from  $\varepsilon_{host}$  to  $\varepsilon_{helix}$  and creates a dielectric function that changes smoothly and allows all field components to be continuous. Equation (6) combined with Eq. (5) provides a way to connect the eigenmodes of a helix array with the eigenmodes of a rod array.

In general, the summation in Eq. (5) becomes exact to the first order of the perturbation, if the original basis is complete and the summation is over all the eigenmodes. In practice, one only needs to include a small number of eigenmodes to achieve a good approximation. Our analysis includes the lowest 6 eigenmodes ( $|E_i^0\rangle$  for j=1,...,6). The average CD indices calculated by the perturbation theory using Eq. (5) and Eq. (6) are shown by the dots in Fig. 5(a). The dots for each band are in an agreement with the respective line in Fig. 5(a), which is the numerically calculated CD indices using MPB simulations. The use of a finite number of eigenmodes in the summation as an approximation is justified by the coupling strength between eigenmodes. In Eq. (5), the coupling term  $\langle E_j^0 | \Delta \varepsilon | E_i^0 \rangle / (\omega_{0,i}^2 - \omega_{0,j}^2)$  determines the coupling strength between the unperturbed eigenmodes  $|E_i^0\rangle$  and  $|E_i^0\rangle$ . Due to the form of the denominator, the strongest couplings are from the eigenmodes that have similar frequencies. Since in the unperturbed system the first TE band and the first TM band have similar frequencies, and moreover these bands have frequencies that are quite different from all the other bands, the first two bands of the helical systems can be well approximated as the hybridization between the first TE and the first TM bands of the unperturbed system. The perturbation theory thus predicts that, as R increases from 0, the first two bands of the helical system should have chirality with similar strength but opposite sign. The prediction agrees quite well with exact numerical simulations of the first two bands in

the helical system as shown in Fig. 5(a). Similar behaviors are also seen for the third and fourth bands of the helical system. As a side note, in applying the perturbation theory of Eq. (5), the complete basis should include longitudinal eigenmodes at  $\omega = 0$ . However, the contribution of such longitudinal eigenmodes is small since the frequency of such eigenmodes are quite far from the other eigenmodes of the unperturbed system.

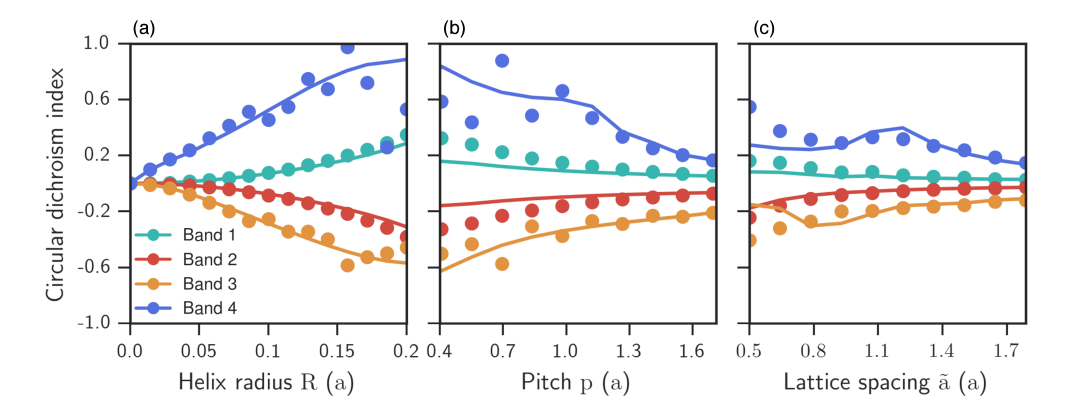


Fig. 5. Comparison of the perturbation theory solution (solid dots) and the direct numerical calculation (lines) of the average CD indices of the first four bands along the  $\Gamma X$  direction for a helix array with r = 0.13a, (a) p = 1.29a and varying R, (b) R = 0.1a and varying p, (c) p = 1.29a, R = 0.1a and varying  $\tilde{a}$ .

In addition to R, p is the second parameter that is effective on chirality. To investigate the effect of p, we apply the same analysis when p is the tuning parameter of chirality and R is fixed to 0.1a. The perturbation theory results and the numerical calculations again agree well as shown in Fig. 5(b). Large values of p make helices more similar to rods, therefore, perturbation theory is more accurate for large p.

We also investigate the effect of the lattice spacing. For this purpose, we denote the lattice spacing as  $\tilde{a}$ , and retain a simply as a length unit. p and R are respectively fixed to 1.29a and 0.1a. As  $\tilde{a}$  varies, we observe smaller changes in the direct numerical calculation of the CD index, as shown by the lines in Fig. 5(c), compared to the changes due to varying R or p, as shown in Fig. 5(a,b). On the other hand, perturbation theory solutions become less accurate for smaller  $\tilde{a}$ . This can be explained by the fact that when helices are placed together a helix is more strongly affected by the perturbation in its neighbors. Therefore, the perturbation becomes stronger as helices come closer and the first-order perturbation results become less accurate.

Finally, we numerically calculate the average CD indices of the first 4 bands for ranges of R and p to understand the dependence on chirality parameters R and p, as shown in Fig. 6. We notice that the behaviors of the bands 1 and 2 are similar to each other while the bands 3 and 4 also share similar characteristics. This similarity is in agreement with the discussion given above. It is also important to mention that the absolute value of the CD index does not monotonically increase with an increase in R or p. Only certain combinations of R and p give the highest absolute value of the CD index.

#### 6. Utilization as a chiral mirror

In previous sections, we provide detailed discussions of the chiral behavior of the structure from the band structure perspective. Remarkably, the strong chiral behavior persists even when we consider the case with only a single layer of helices, for which the structure becomes a metasurface. In Fig. 7 we show the reflectance and transmittance of this metasurface for normally

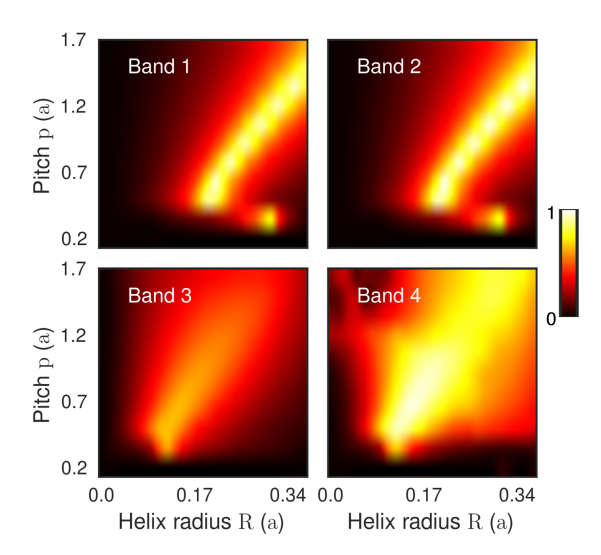


Fig. 6. The absolute value of the average CD index as a function of p and R for the first four bands for the structure in Fig. 1 along the  $\Gamma X$  direction.

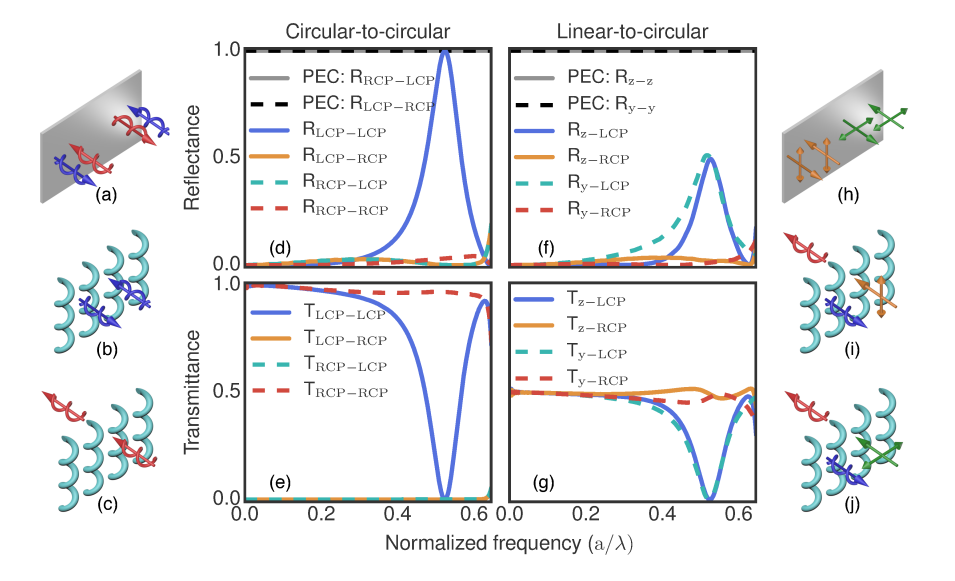


Fig. 7. The intensity reflectance ((d) and (f)), and transmittance ((e) and (g)) spectra for the incident wave with circular polarization ((d) and (e)) and linear polarization ((f) and (g)). (a), (b) and (c) illustrate how circularly polarized incident waves interact with an ordinary mirror and a helix metasurface. (h), (i) and (j) illustrate how linearly polarized incident waves interact with an ordinary mirror and a helix metasurface.

incident light with either linear or circular polarizations. Strong reflection is observed near the frequency of  $0.53a/\lambda$ . Near this frequency, for left-handed circularly polarized incident waves, the reflected wave is also circularly polarized with the same handedness. This is in contrast to a reflection off of an conventional metallic mirror where the handedness flips upon reflection. For linearly polarized incident light, the reflected light has left-handed circular polarization regardless

of the direction of the incident linear polarization. Similar handedness-preserving mirrors, or chiral mirrors, have been previously achieved either with metallic structures or with dielectric photonic crystal slab structures at off-normal incidence [23–25]. There are various applications proposed for chiral mirrors such as reflective circular polarizers, bolometers and self-polarizing cavities [23]. Here our work provides a realization of a dielectric chiral mirror for normal incident light.

#### 7. Conclusion

In summary, we have shown that there are strong effects of circular dichroism and polarization stop gaps in dielectric helices for light propagating along a direction perpendicular to the helices, despite the nonexistence of helical symmetry along this direction. We have used band structure analysis and finite-difference time-domain simulations to demonstrate these effects. We have also presented a quantitative discussion using perturbation theory to explain how these effects emerge. Finally, we have shown that strong circular dichroism effects persist even for a single layer of helices such that it reflects one circular polarization 100% while completely transmitting the other. Such reflection moreover preserves the handedness of the incident light's polarization, unlike a regular mirror in which handedness flips upon reflection. We have thus shown that such a structure behaves as a chiral mirror. The work here should motivate further explorations of dielectric helix structures for various applications.

#### **Funding**

Air Force Office of Scientific Research MURI program (FA9550-12-1-0471); National Science Foundation (NSF) (CBET-1641069).

#### **Acknowledgments**

The authors would like to acknowledge the discussions with Prof. John A. Rogers, and his group members Philipp Gutruf, Zheng Yan and Mengdi Han.